

# Hybrid Simulation Codes: Past, Present and Future – A Tutorial

Dan Winske<sup>1</sup>, Lin Yin<sup>1</sup>, Nick Omidi<sup>2,3</sup>, Homa Karimabadi<sup>2</sup>, and Kevin Quest<sup>2</sup>

<sup>1</sup> Applied Physics Division, Los Alamos National Laboratory, Los Alamos, NM 87545  
USA *winske@lanl.gov*, *lyin@lanl.gov*

<sup>2</sup> Electrical and Computer Engineering Department, University of California San  
Diego, La Jolla, CA 92093 USA *nomidi1@san.rr.com*

<sup>3</sup> California Space Institute, University of California San Diego, La Jolla, CA 92093  
USA

**Abstract.** Hybrid codes, in which the ions are treated kinetically and the electrons are assumed to be a massless fluid, have been widely used in space physics over the past two decades. These codes are used to model phenomena on ion inertial and gyro-radius scales, which fall between longer scales obtained by magnetohydrodynamic simulations and shorter scales attainable by full particle simulations. In this tutorial, the assumptions and equations of the hybrid model are described along with some most commonly used numerical implementations. Modifications to include finite electron mass are also briefly discussed. Examples of results of two-dimensional hybrid simulations are used to illustrate the method, to indicate some of the tradeoffs that need to be addressed in a realistic calculation, and to demonstrate the utility of the technique for problems of contemporary interest. Some speculation about the future direction of space physics research using hybrid codes is also provided.

## 1 Hybrid Codes: Past

Generally, the term “hybrid code” in plasma physics can refer to any simulation model in which one or more of the plasma species are treated as a single or multiple fluids, while the remaining species are treated kinetically as particles. The plasma can be coupled to the electromagnetic fields in a variety of ways: full Maxwell equations, low-frequency magnetostatic (Darwin) model, electrostatic only, etc. In this tutorial, we shall concentrate mainly on the most common type of hybrid code used in space plasmas: where all the ions are treated kinetically, the electrons are assumed to be an inertia-less and quasi-neutral fluid, and the electromagnetic fields are treated in the low-frequency approximation. Some comments on the extension to finite electron mass hybrid algorithms will also be made.

Because this tutorial is being presented in the context of the International School for Space Simulation (ISSS), we will mostly restrict the discussion of “past” uses of hybrid methods in space physics to the articles published in the previous schools. Those articles give appropriate and timely references to research that was carried out at that time with hybrid codes that were then available.

In the same vein, in this tutorial the principal focus will be on numerical implementations of the hybrid model that are presently being used, and similarities and differences among the various algorithms. Numerical examples are discussed, in the context of some research questions currently being investigated with hybrid codes. This is the subject of Sect. 2: Hybrid codes – present.

Simulation codes with particle ions and fluid electrons appeared in the early 70's. Auer et al. [1] treated the ions as charged sheets and studied shocks and associated heating in relation to the Earth's bow shock. Forslund and Freidberg [2] and Mason [3] modeled shocks with unmagnetized ions treated by the particle-in-cell method. Chodura [4] wrote the first true “hybrid” code in the sense described above and applied it to laboratory pinch experiments. The hybrid model was subsequently used by Sgro and Nielson [5] and Hamasaki et al. [6] for related types of experiments. A 2-D version of the model was worked out by Hewett [7]. Leroy et al. [8] then adopted the Sgro and Nielson algorithm to model the structure of the bow shock. From there, the variations of algorithms and applications for space physics grew rapidly, as discussed later in this paper.

Hybrid codes have been well represented in the publications from the previous Simulation Schools. One-dimensional hybrid algorithms are discussed in some detail in the articles from the first [9] and second [10] schools. These articles emphasize applications to collisionless shocks and low-frequency waves in the ion foreshock. At the third school, Quest [11] discussed hybrid codes more generally, comparing and contrasting several multi-dimensional hybrid algorithms. As we will see, the field has not advanced much beyond what was described in that article. Winske and Omid [12] presented a tutorial on hybrid codes at the fourth school that once again emphasized, for pedagogical reasons, one-dimensional codes. In this case, ion beam instabilities were used to illustrate the main features of hybrid simulation methods. Given that rather complete treatment, the emphasis in this tutorial will be on two-dimensional implementations and applications. These applications include ion beam instabilities, magnetic reconnection, and global hybrid simulations of the solar wind-magnetosphere interaction. Students and young researchers who are not familiar with hybrid techniques are urged to consult that ISSS-4 article as a reference point to the following discussion. The Winske and Omid tutorial concluded with an outlook of how hybrid codes might evolve in future years. We will use that discussion as the basis for gauging progress over the past ten years as well as for making another prediction for the years ahead in Sect. 3: Hybrid codes – future.

Hybrid codes are also discussed in other articles in this volume, based on the tutorials given at ISSS-6. In particular, Pritchett [13] presents a very lucid tutorial on particle-in-cell methods generally and discusses the hybrid model in the context of other plasma kinetic models. Articles in the proceedings of ISSS-6 also consider a number of current applications of hybrid codes [14]–[18].

While the emphasis here is on work presented at ISSS, we also note three recent review articles that are also of interest. Winske and Omid [19] discussed the general issue of the use of kinetic simulations in space plasmas and what type of simulation model (full particle, hybrid, etc.) is most appropriate under

various conditions. The strengths and weaknesses of kinetic simulation methods in general are discussed and some guidance on how to discern between “good” and “bad” simulations is provided. A more recent review of simulation methods and space physics applications is given by Pritchett [20]. Omura et al. [21] summarized relevant work on nonlinear kinetic processes in space plasmas in the recent URSI quadrennial report. It discusses results of observations, theory and simulations for a wide variety of phenomena and contains results from a number of hybrid simulations. On rereading this article, what strikes us most significantly is how simulations, whether they be full particle, hybrid, or MHD, have become so intermeshed with theory and observations in space physics. When ISSS was established, this was the principal goal. We have often failed to realize how well we have achieved this objective in the last twenty years.

Hybrid codes with finite electron mass are an interesting extension. This subject has been covered in depth in a recent monograph [22] that also considers inertia-less hybrid models. Given that extensive treatment, we will present only a brief discussion of this modification in the middle of Sect. 2. We have not included any discussion of hybrid codes that treat the electrons implicitly, which allows inertia and/or kinetic effects to be easily added in [23], or that deal with electrostatic phenomena [24]. If the scope of the readers’ interests extends beyond the narrow confines of this tutorial, we urge them to consult these other references, as well as the magnetic (e.g., in [25] and [26]), and inertial fusion [27] literature.

## 2 Hybrid Codes: Present

### 2.1 Basic Assumptions and Equations

Hybrid codes arise from the need to model phenomena that occur on shorter time and distance scales than can be treated by magnetohydrodynamics and yet do not resolve processes that occur on electron scales (e.g., electron gyro-radius and electron Debye length scales, inverse electron gyrofrequency and electron plasma frequency time scales). The relevant scales are then the ion gyro-radius and ion inertial spatial scales, and inverse ion gyrofrequency time scale. In space, these length scales typically are on the order of 10’s to 100’s of km and times on the order of seconds; these ion scales are readily resolved by satellite instrumentation. To model phenomena on these scales with a hybrid code, as contrasted with a Hall-MHD code, implies assumptions about the descriptions of the plasma ions and electrons as well as the electromagnetic fields.

To be consistent with the hybrid model, the ions are treated kinetically, i.e., using standard particle-in-cell techniques [12][13][20][28]. Each simulation ion (charge  $q_i$ , mass  $m_i$ ) is subject to the usual equations of motion:

$$m_i \frac{d\mathbf{v}_\mathbf{p}}{dt} = q_i (\mathbf{E} + \frac{\mathbf{v}_\mathbf{p} \times \mathbf{B}}{c}), \quad (1)$$

$$\frac{d\mathbf{x}_\mathbf{p}}{dt} = \mathbf{v}_\mathbf{p}, \quad (2)$$

where  $\mathbf{E}$  and  $\mathbf{B}$ , which have values given on a spatial grid, are the electric and magnetic fields interpolated to the particle location. The updated particle information is collected at the grid points to determine the ion number density ( $n_i$ ), charge density ( $q_i n_i$ ), flow velocity  $\mathbf{V}_i$  and current  $\mathbf{J}_i = q_i n_i \mathbf{V}_i$ . (We will assume one ion species throughout. For multiple species, one accumulates the quantities for each species separately and then adds them together to determine the total ion charge density and current.)

In order to eliminate kinetic electron effects, the electrons are treated as an inertia-less fluid ( $m_e = 0$ ). The electron momentum equation is thus:

$$n_e m_e \frac{d\mathbf{V}_e}{dt} = 0 = -en_e(\mathbf{E} + \frac{\mathbf{V}_e \times \mathbf{B}}{c}) - \nabla \cdot \underline{\mathbf{P}}_e, \quad (3)$$

where  $\mathbf{V}_e$  is the electron fluid velocity and  $\underline{\mathbf{P}}_e$  is the electron pressure tensor. Ignoring effects on the electron Debye length scale further implies that the plasma is quasi-neutral, so that the electron and ion charge densities are equal:

$$en_e = q_i n_i, \quad (4)$$

where the electron charge is  $-e$  and  $n_e$  is the electron number density. In Eq. (3),  $\underline{\mathbf{P}}_e$  is almost always taken as a scalar,  $\underline{\mathbf{P}}_e = p_e \mathbf{1}$ . Typically, an isothermal or adiabatic relation between the pressure and temperature is assumed. For simplicity, we have also left off resistive coupling between the electrons and ions; this adds a term  $en_e \underline{\eta} \cdot \mathbf{J}$  to the right-hand side of (3), where  $\mathbf{J}$  is the total current. The resistivity  $\underline{\eta}$  is usually taken as a scalar with a constant coefficient. For momentum conservation, it requires adding  $-e \underline{\eta} \cdot \mathbf{J}$  to the acceleration term in the ion particle equation of motion (1) as well. We will return to the issues of the electron pressure tensor and the resistivity later.

Finally, the electromagnetic fields are treated in the low frequency approximation: Ampere's law,

$$\nabla \times \mathbf{B} = \frac{4\pi}{c} \mathbf{J} = \frac{4\pi}{c} q_i n_i (\mathbf{V}_i - \mathbf{V}_e), \quad (5)$$

using (4), and Faraday's law

$$\frac{\partial \mathbf{B}}{\partial t} = -c(\nabla \times \mathbf{E}). \quad (6)$$

As is done in two-fluid codes, Eq. (5) is used to eliminate  $\mathbf{V}_e$  in (3) and Eq. (6) is used to advance the magnetic field in time. Because  $m_e = 0$ , Eq. (3) can be solved for the electric field directly, so that no time advance of  $\mathbf{E}$  is needed. The other Maxwell's equations, e.g., Poisson's equation,  $\nabla \cdot \mathbf{E} = 4\pi(q_i n_i - en_e)$ , is satisfied by virtue of the quasi-neutral approximation (4) and boundary conditions; likewise  $\nabla \cdot \mathbf{B} = 0$  is also satisfied.

Further discussion of the underlying assumptions of the hybrid model is given in papers describing the various hybrid algorithms, which we will consider in the next subsection.

## 2.2 Numerical Implementations

The numerical implementation of the hybrid model in a simulation code is relatively straightforward. However, as we shall see, one piece is not entirely there, which leads to various ways to circumvent this problem. Hybrid codes in space are usually (but not always, e.g., in [29]), done on a rectangular grid. Usually, a staggered pair of grids is used, with the electric field, plasma density, current, and pressure located on the vertices of one grid, and the magnetic field on the vertices of the other grid. This implies that  $\text{curl } \mathbf{E}$  will be given properly on the B-grid, while  $\text{curl } \mathbf{B}$  will be correct at the location of the electric field.

Given this grid, the ion dynamics are done as in any PIC code: the fields are interpolated to the particles' positions to give the correct acceleration and after the ions are moved, the density and current can be redeposited back to the grid [12][13][20][28]. Typically, linear weighting is used; higher order splines have also been employed. As usual, the particle positions and velocities are leapfrogged in time. In other words, at time step  $N$  (denoted by the superscript), the particle positions  $\mathbf{x}_p^N$  and the fields  $\mathbf{E}^N$  and  $\mathbf{B}^N$  are known, while the particle velocities are known at the half-time step,  $N - 1/2$ . Given  $\mathbf{E}^N$  and  $\mathbf{B}^N$ , at the beginning of the time step, the velocities can be advanced to time level  $N + 1/2$  and the particle positions to time step  $N + 1$ :

$$\mathbf{v}_p^{N+1/2} = \mathbf{v}_p^{N-1/2} + \frac{q_i}{m_i}(\mathbf{E}^N + \frac{\mathbf{v}_p^N \times \mathbf{B}^N}{c})\Delta t, \quad (7)$$

$$\mathbf{x}_p^{N+1} = \mathbf{x}_p^N + \mathbf{v}_p^{N+1/2}\Delta t. \quad (8)$$

In the process the currents are collected at  $N + 1/2$  and the density at  $N + 1$ . Note that Eq. (7) is implicit in  $\mathbf{v}_p^{N+1/2}$ , as  $\mathbf{v}_p^N$  can be written as  $1/2(\mathbf{v}_p^{N-1/2} + \mathbf{v}_p^{N+1/2})$  (see Appendix A in [12]).

Most hybrid codes solve the field equations explicitly in time, although implicit methods do exist [7][15][22]. In an explicit scheme, the straightforward way to advance the fields is to use Faraday's law (6) and  $\mathbf{E}^N$  to advance the magnetic field to level  $N + 1/2$

$$\mathbf{B}^{N+1/2} = \mathbf{B}^N - \frac{c\Delta t}{2}(\nabla \times \mathbf{E}^N). \quad (9)$$

Recall that the electron momentum equation (3) can be solved for the electric field, which using (5), can be written as

$$\begin{aligned} \mathbf{E}^{N+1/2} &= -\frac{\mathbf{V}_i^{N+1/2} \times \mathbf{B}^{N+1/2}}{c} - \frac{\nabla p_e^{N+1/2}}{q_i n_i^{N+1/2}} - \frac{\mathbf{B}^{N+1/2} \times (\nabla \times \mathbf{B}^{N+1/2})}{4\pi q_i n_i^{N+1/2}} \\ &= \mathbf{F}(\mathbf{B}^{N+1/2}, n_i^{N+1/2}, \mathbf{V}_i^{N+1/2}). \end{aligned} \quad (10)$$

Since we have the ion current and the magnetic field at time level  $N + 1/2$ , and the density (either collected directly at  $N + 1/2$  or use the average between values at  $N$  and  $N + 1$ ), we have all the information needed to evaluate  $\mathbf{E}^{N+1/2}$ .

With the newly evaluated  $\mathbf{E}^{N+1/2}$ , again Faraday's law can be used to push  $\mathbf{B}$  to time level  $N + 1$

$$\mathbf{B}^{N+1} = \mathbf{B}^{N+1/2} - \frac{c\Delta t}{2}(\nabla \times \mathbf{E}^{N+1/2}). \quad (11)$$

However, the advance of  $\mathbf{E}$  from time level  $N + 1/2$  to  $N + 1$  is not so straightforward. An examination of (10) shows that  $\mathbf{B}^{N+1}$  and  $n_i^{N+1}$  are known, but not  $\mathbf{V}_i^{N+1}$ . The problem of implementing a good algorithm for hybrid codes that reduces to how to best calculate  $\mathbf{E}^{N+1}$ . Much of the rest of this subsection is devoted to discussing various ways that this has been accomplished.

Historically the first method, which continues to be widely used, is a predictor-corrector technique [30]–[33]. The basic idea is to: (i) make a prediction of the fields (denoted by primes) at  $N + 1$ ; (ii) advance the particles in the predicted fields in order to compute the ion source terms at time level  $N + 3/2$ ; (iii) use that current (and charge density) to compute predicted fields at  $N + 3/2$ ; and (iv) use the average of the electric field at  $N + 1/2$  and the predicted field at  $N + 3/2$  to get  $\mathbf{E}^{N+1}$ . In equation form, this procedure becomes the following four steps [31][32]:

(i) the predicted fields

$$\mathbf{E}'^{N+1} = -\mathbf{E}^N + 2\mathbf{E}^{N+1/2}, \quad (12)$$

$$\mathbf{B}'^{N+1} = \mathbf{B}^{N+1/2} - \frac{c\Delta t}{2}(\nabla \times \mathbf{E}'^{N+1}); \quad (13)$$

(ii) advance the particles to obtain predicted source terms,  $\mathbf{V}_i^{N+3/2}$ ,  $n_i^{N+3/2}$ ;  
 (iii) compute the predicted fields at  $N + 3/2$

$$\mathbf{B}'^{N+3/2} = \mathbf{B}'^{N+1} - \frac{c\Delta t}{2}(\nabla \times \mathbf{E}'^{N+1}), \quad (14)$$

$$\mathbf{E}'^{N+3/2} = \mathbf{F}(\mathbf{B}'^{N+3/2}, n_i^{N+3/2}, \mathbf{V}_i^{N+3/2}); \quad (15)$$

(iv) Determine corrected fields at  $N + 1$

$$\mathbf{E}^{N+1} = \frac{1}{2}(\mathbf{E}^{N+1/2} + \mathbf{E}'^{N+3/2}), \quad (16)$$

$$\mathbf{B}^{N+1} = \mathbf{B}^{N+1/2} - \frac{c\Delta t}{2}(\nabla \times \mathbf{E}^{N+1}). \quad (17)$$

In principle, the process could be repeated to improve the accuracy, but in practice this is almost never done. This method is still often used because it gives very good energy conservation and is rather robust. As we shall see later, however, there can be significant amount of short wavelength whistler noise generated by the application of this technique, which will require additional

measures to remove. It is evident that this technique will be somewhat slow, since one has to move the particles twice each time step. Less evident at this point in the discussion is that the short wavelength noise problem may also require a somewhat smaller time step.

The second type of method to advance the electric field to time level  $N + 1$  is an extrapolation of the ion flow velocity (or equivalently the ion current density) from  $N + 1/2$  to  $N + 1$  [34][35]. Since the other quantities are known at  $N + 1$  already, with an extrapolated  $\mathbf{V}_i^{N+1}$ ,  $\mathbf{E}^{N+1}$  can be directly evaluated, and the time-stepping process can proceed to the next cycle. Intuitively this method may not be as accurate, but it is better than one might expect, as we will show quantitatively later when we discuss some simple examples, and is often used for many problems.

The extrapolation of the ion velocity can be done in several ways. First, by merely using the saved values of  $\mathbf{V}_i^{N-1/2}$  and  $\mathbf{V}_i^{N+1/2}$ , one has [35]:

$$\mathbf{V}_i^{N+1} = \frac{3}{2}\mathbf{V}_i^{N+1/2} - \frac{1}{2}\mathbf{V}_i^{N-1/2}. \quad (18)$$

One can also keep  $\mathbf{V}_i^{N-3/2}$  to improve the accuracy, so that the process becomes a 4th order Bashford-Adams extrapolation, which is the way this method was first introduced [34]:

$$\mathbf{V}_i^{N+1} = 2\mathbf{V}_i^{N+1/2} - \frac{3}{2}\mathbf{V}_i^{N-1/2} + \frac{1}{2}\mathbf{V}_i^{N-3/2}. \quad (19)$$

Alternatively, one can follow the philosophy of implicit plasma methods and advance a moment equation to give a better estimate of the ion current [11]. This method requires accumulating the ion pressure tensor and may need some additional enhancement for multi-ion species problems, but it has shown promise [36]:

$$\begin{aligned} \mathbf{V}_i^{N+1} = & \mathbf{V}_i^{N+1/2} - \frac{\Delta t}{2}(\mathbf{V}_i \cdot \nabla \mathbf{V}_i)^{N+1/2} \\ & + \frac{\Delta t}{2m_i n_i^{N+1/2}}(-\nabla p_e^{N+1/2} - \nabla \cdot \mathbf{P}_i^{N+1/2} + \frac{\mathbf{J}^{N+1/2} \times \mathbf{B}^{N+1/2}}{c}). \end{aligned} \quad (20)$$

However, this method requires the accumulation of the ion pressure tensor and the evaluation of an advective derivative, which would seem to negate main advantages of using a hybrid code that has particles to calculate the effects of  $\mathbf{P}_i$  and the advection already.

In the CAM-CL method, which has become popular in recent years, the ion current is calculated by doing an extra half time step push using a mixed level evaluation of the electric field [37]:

$$\mathbf{V}'_i^{N+1} = \mathbf{V}_i^{N+1/2} + \frac{q_i \Delta t}{m_i 2}(\mathbf{E}^* + \frac{\mathbf{V}_i^{N+1/2} \times \mathbf{B}^{N+1}}{c}), \quad (21)$$

$$\mathbf{E}^* = \mathbf{F}(\mathbf{B}^{N+1}, n_i^{N+1}, \mathbf{V}_i^{N+1/2}). \quad (22)$$

Note that here, as in all of these extrapolation methods, only one push of the ions each time step is required.

There are also several other hybrid algorithms, which require iterations. The Horowitz algorithm [38] solves the following (time-centered) set of field equations iteratively for  $\mathbf{E}^{N+1}$  and  $\mathbf{B}^{N+1}$ , given the source terms at time level  $N+1/2$ :

$$\mathbf{B}^{N+1} = \mathbf{B}^N - \frac{c\Delta t}{2}(\mathbf{E}^N + \mathbf{E}^{N+1}), \quad (23)$$

$$\mathbf{E}^{N+1} = -\mathbf{E}^N + \frac{1}{2}\mathbf{F}\left(\frac{\mathbf{B}^N + \mathbf{B}^{N+1}}{2}, n_i^{N+1/2}, \mathbf{V}_i^{N+1/2}\right). \quad (24)$$

One starts the iteration by assuming  $\mathbf{E}^{N+1} = \mathbf{E}^N$ ; typically 5-10 iterations are needed to give convergence.

Another iteration method involves a combination of the velocity extrapolation and predictor corrector [39]. After the velocity is estimated to calculate  $\mathbf{E}^{N+1}$ , the particles can be moved in the new fields to give a better estimate for  $\mathbf{V}_i^{N+1}$  that can then be used to recompute  $\mathbf{E}^{N+1}$ ; the system can be iterated until the  $\mathbf{E}^{N+1}$  is in some sense converged.

While the emphasis here so far has been on the advance of the electric field, it should also be noted that there have improvements in advancing the magnetic field. Because of the generation of short wavelength whistlers, the time step restricting the advance of the magnetic field is smaller than that for the ions (which is a small fraction of the ion gyroperiod). Writing Faraday's law (6) in terms of the electric field (10), we have

$$\frac{\partial \mathbf{B}}{\partial t} = -c(\nabla \times \mathbf{E}) = \nabla \times \mathbf{F}(\mathbf{B}, n_i, \mathbf{V}_i). \quad (25)$$

The quantities on the right-hand side are all evaluated at time level  $N+1/2$ , except for  $\mathbf{B}$ . One can then advance this equation from  $N$  to  $N+1$  with  $\mathbf{B}$  on the right-hand side changing, using a 4th-order Runge-Kutta scheme [39]; i.e., (suppressing the last two arguments of  $\mathbf{F}$ )

$$\mathbf{B}^{N+\theta} = \mathbf{B}^N + \frac{\Delta t'}{6}(\mathbf{K}_1^N + 2\mathbf{K}_2^N + 2\mathbf{K}_3^N + \mathbf{K}_4^N), \quad (26)$$

$$\mathbf{K}_1^N = -\nabla \times \mathbf{F}(\mathbf{B}^N), \quad (27)$$

$$\mathbf{K}_2^N = -\nabla \times \mathbf{F}(\mathbf{B}^N + \frac{\Delta t'}{2}\mathbf{K}_1^N), \quad (28)$$

$$\mathbf{K}_3^N = -\nabla \times \mathbf{F}(\mathbf{B}^N + \frac{\Delta t'}{2}\mathbf{K}_2^N), \quad (29)$$

$$\mathbf{K}_4^N = -\nabla \times \mathbf{F}(\mathbf{B}^N + \Delta t'\mathbf{K}_3^N), \quad (30)$$

using a subcycled time interval,  $\Delta t' = \Delta t/\theta$ .

Another approach that is used in the CAM-CL algorithm is to keep two copies of the magnetic field, one at the full time step and one at the half time



step and leapfrog these along in time, again subcycling if needed [37]. The two field solutions can be averaged after a given number of time steps.

Finally, it should be mentioned that if one ignores the electron pressure, the electric field can be eliminated entirely, resulting in a simpler algorithm [40]. This method is noteworthy in that a Richardson extrapolation (to  $\Delta t \rightarrow 0$ ) is used in the particle velocity advance equation to dramatically improve the energy conservation. Two solutions, one advanced one time step ( $\Delta t$ ) and the other advanced two half time steps ( $\Delta t/2$ ) are compared and used to determine what the particle velocity at the next time step should actually be. But this is somewhat expensive, as two sets of particles are needed.

Before going on to numerical examples, we digress a bit to discuss hybrid codes with finite electron mass. The inclusion of electron inertia changes the whistler dispersion relation at short wavelengths, so that the real frequency no longer varies as the square of the wavenumber. If one is interested in resolving spatial scales that are a small fraction of the ion inertial length, this change of the wave phase velocity can reduce numerical problems at short wavelengths, so that one may wish to consider including  $m_e \neq 0$  effects. There are several ways that this can be accomplished. The recently published monograph by Lipatov [22] is an excellent reference where the details can be found.

Hewett and Nielson [41] include electron inertia effects by a process that involves separating the electron current into its longitudinal (curl-free) and transverse (divergence-free) components. An equation for the total current can be obtained by summing the electron and ion momentum equations. Taking the divergence of this summed equation, and using the quasi-neutral condition expressed as  $\nabla \cdot \mathbf{J} = 0$ , one obtains an expression that can be solved for the longitudinal electric field, i.e., a generalized Poisson's equation for quasi-neutral plasmas. In similar fashion, the longitudinal part of the electron current, being curl-free, can be expressed as a scalar potential,  $\mathbf{J}_{el} = -\nabla V$ . The divergence of this expression yields a Poisson equation,  $\nabla^2 V = -\nabla \cdot \mathbf{J}_{el} = -\nabla \cdot \mathbf{J}_l = \nabla \cdot \mathbf{J}_i$ ; the right-hand side is evaluated directed from the particle ions. Thus, knowing the total current, the ion current, and the longitudinal electron current, one easily obtains the electron transverse current ( $\mathbf{J}_{et}$ ).  $\mathbf{J}_{et}$  is advanced in time and used to calculate the vector potential  $\mathbf{A}$  (or alternatively the time derivative of  $\mathbf{J}_{et}$  is advanced and used to directly calculate the transverse electric field  $\mathbf{E}_t$ ). The method is straightforward, but a number of Poisson solves are needed to separate the transverse and longitudinal parts of the current and calculate the electric field.

In recent years, it has become more common to include electron inertia effects solving a set of generalized field equations [15]. One derives this set of equations from (3), but where the left-hand side is not set to zero, along with Eq. (6), by assuming:

$$\hat{\mathbf{B}} = \mathbf{B} - \delta_e^2 \nabla^2 \mathbf{B}, \quad \delta_e = (c^2 m_e / 4\pi e^2)^{1/2} \quad (31)$$

and taking the curl of Eq. (3) to give

$$\frac{1}{c} \frac{\partial \hat{\mathbf{B}}}{\partial t} = -(\nabla \times \hat{\mathbf{E}}), \quad (32)$$

where

$$\hat{\mathbf{E}} = -\frac{\mathbf{V}_e \times \mathbf{B}}{c} - \frac{\nabla \cdot \mathbf{P}_e}{en_e} - \frac{m_e}{e} (\mathbf{V}_e \cdot \nabla) \mathbf{V}_e. \quad (33)$$

This set of equations is not exact; we have dropped terms proportional to  $m_e \partial n_e / \partial t$  and  $m_e \partial \mathbf{V}_i / \partial t$ . It is argued that on short, electron spatial scales, the ions are nearly immobile and the neglected density and ion velocity variations are small [15][22][42][43]. The nice feature of Eqs. (31–33) is that one again has one equation for the time advance of the (generalized) magnetic field and a second equation for the (generalized) electric field that does not contain an explicit time derivative. These equations can be advanced in time using the same methods discussed previously.

Finite electron mass hybrid codes have been applied to a variety of problems, ranging from instabilities, e.g., the lower hybrid drift instability [41], collisionless shocks and solar wind-comet interactions [15][22], and magnetic reconnection [42][43]. The various calculations show the need to include finite electron mass to excite some instabilities, to generate strong whistler turbulence at shocks, and to show the role of short-scale physics in the reconnection process. It should be noted, however, that the fluid electron approximation eliminates electron Landau damping that tends to suppress whistler growth at short wavelengths. Thus, one may still want to use additional smoothing or some resistivity (but keeping the resistive length small compared to the cell size) to reduce the amplitude of the short wavelength fluctuations. And the generalized equations for solving for the electromagnetic fields with  $m_e \neq 0$  should be compared with solutions of the full equations [41] for realistic test problems to check that the neglect of some of the time-dependent ion terms is indeed valid.

We emphasize that all of the methods discussed in this section work with various degrees of success that may also depend on the problem under consideration. It is best to keep several algorithms in your toolbox and try them all out when encountering a new application.

## 2.3 Examples

We next compare results from hybrid simulations based on two commonly used hybrid algorithms for a simple test problem. We show the potential tradeoff of speed versus accuracy. We go on to discuss the issue of short wavelength whistler noise and ways to suppress it. We also discuss a more complex test problem (reconnection in 2-D), comparing results from hybrid and Hall-MHD simulations. The possible use of hybrid techniques for more global problems raises enough issues that we will consider it in a separate section (2.4 Global Hybrid Calculations).

For the first comparison, we use two versions of the hybrid code we employ at Los Alamos. One version uses the standard predictor corrector scheme. The other uses velocity extrapolation along with a subcycled advance of the magnetic field using a 4th-order Runge-Kutta integration. We consider relatively small systems ( $128 \times 128$  cells, 50 particles per cell) with periodic boundary conditions to provide some illustrative comparisons. The test problem concerns the excitation of unstable, oblique Alfvén/ion cyclotron waves driven by cold, relatively slow ion beams that are found in the plasma sheet boundary layer and the solar wind [44]–[48]. These waves appear in the upstream region of slow shocks in the magnetotail and can be responsible for ion heating that occurs both upstream and in the shock transition. They also can provide ion heating in the solar wind. For this problem, results of two-dimensional simulations are shown in order to compare plasma and wave quantities and the effect of varying numerical parameters.

Specifically, we assume two equal density ion beams streaming relative to each other along the magnetic field ( $x$ -direction) with velocities of  $\pm V_A$  (the Alfvén velocity based on the total ion density). The beams have  $\beta_{i\parallel} = \beta_{i\perp} = 0.025$  (with  $\beta$  based on the total ion density, and parallel and perpendicular are in reference to the magnetic field direction), and  $T_e = T_i$ , with the electrons treated adiabatically with  $\gamma = 5/3$ . The system length in both the  $x$  and  $y$  directions is  $48c/\omega_i$  with  $\omega_i$  the ion plasma frequency based on the total ion density. The calculations employ  $128 \times 128$  cells, with 25 particles per cell for each ion species. The simulations use a resistivity (normalized to  $4\pi/\omega_i$ ), usually  $\eta = 10^{-6}$ , corresponding to a resistive length about 1% of the cell size. In the velocity extrapolation runs, the time step is  $\Omega_i \Delta t = 0.05$  ( $\Omega_i$  is the ion gyrofrequency); the predictor-corrector runs require a smaller time step,  $\Omega_i \Delta t = 0.02$ , because of the persistence of short wavelength fluctuations. The predictor-corrector simulation smooths the source term during both the predictor and corrector cycles; the velocity extrapolation simulation smooths the source terms once or twice each time step. To obtain the smoothed value of a quantity at each grid point, we take one-quarter of the original value plus one eighth of the values of the four nearest neighbors and one-sixteenth of the values of the next four nearest neighbors.

Figure 1 shows results of two hybrid simulations comparing the velocity extrapolation (solid curves) and predictor/correct (dashed curves) algorithms. Plotted are time histories of the magnetic field fluctuations in the top panel (normalized to the ambient magnetic field) and the parallel and perpendicular ion temperatures (normalized to their initial values) in the middle panel. The magnetic fluctuations grow exponentially, saturate a modest level,  $(\delta B/B_o)^2 \simeq 0.08$ , oscillate, and then eventually decay. The ions are heated strongly in the perpendicular temperature, and much less in the parallel direction, consistent with earlier 1-D and 2-D simulations of this instability [45]. The power spectra of the fluctuations at  $\Omega_i t = 100$  as a function of  $k_x$  are shown in the bottom panel. The spectra exhibit a broad peak of waves at long wavelength, with a steady fall-off at higher wavenumbers. The unstable waves grow slightly earlier in time in the predictor-corrector run, and show similarly time-shifted nonlinear oscillations

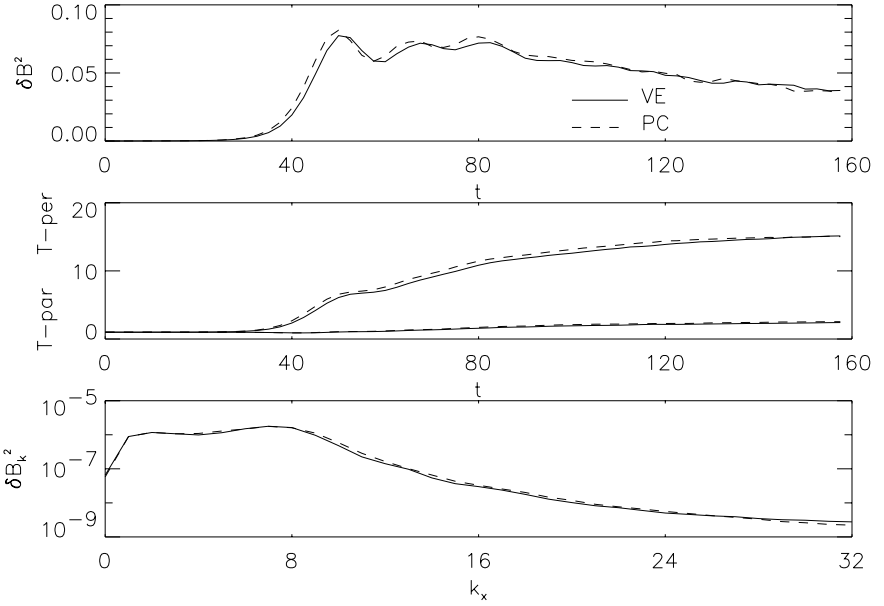


**Fig. 1.** Results of simulations of the Alfvénion beam instability comparing a velocity extrapolation algorithm (solid curves) with a predictor/corrector algorithm (dashed curves), showing magnetic field fluctuations (top panel), parallel and perpendicular ion temperatures (middle panel), both as a function of time, and power spectra of the magnetic fluctuations as a function of  $k_x$  at  $\Omega_i t = 100$ . Both calculations use the same normalized resistivity,  $\eta = 10^{-6}$ .

after saturation. The predictor-corrector run also shows slightly more perpendicular ion heating and a slight enhancement to the fluctuation level (except at the shortest wavelengths where it is reduced by the extra smoothing in this case).

Figure 2 compares profiles of the  $B_z$  magnetic field component (normalized to  $B_o$ ) versus  $x$  at  $y = L_y/2$  at various times for these simulations. At  $\Omega_i t = 50$ , at the end of the period of exponential wave growth, the wave profiles are regular in shape and very similar in the two calculations. By  $\Omega_i t = 100$ , the instability is into the nonlinear stage, but one can still see correspondence between the various peaks in the wave profiles, which have evolved into rather complex wave-forms. At  $\Omega_i t = 150$ , the wave spectra are evidently dominated by longer wavelength modes and the correspondence between individual peaks has been phase-mixed away to a large degree.

Figure 3 compares results for various velocity extrapolation runs in which the resistivity and/or the smoothing is changed. The solid curves correspond to the same case as shown in Fig. 1. In this run, the normalized resistivity is  $\eta = 10^{-6}$  and the source terms are smoothed once each time step. A second run in which a second smoothing operation is included each time step is shown as the dashed lines. In this case, the excitation and growth of the fluctuations

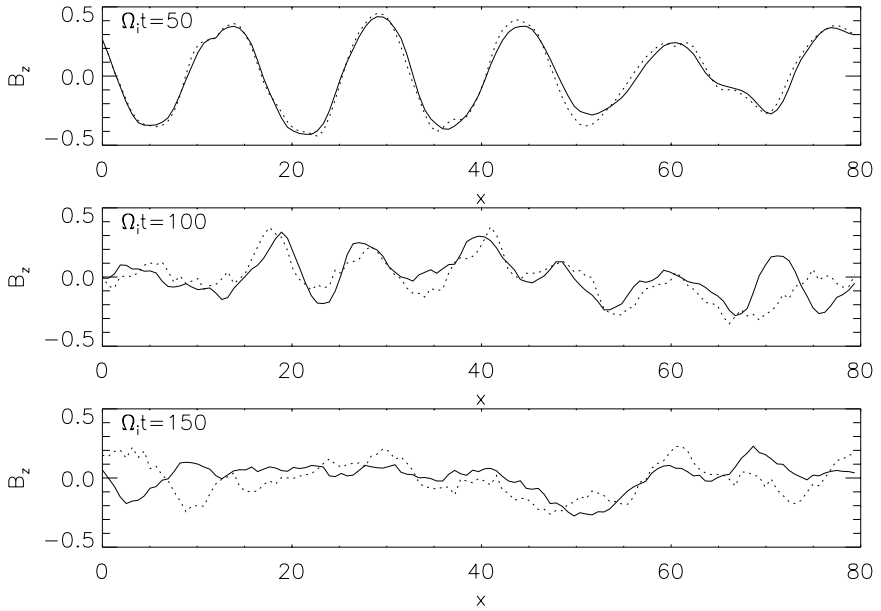


**Fig. 2.** Further results of the simulations given in Fig. 1, showing profiles of  $B_z$  versus  $x$  at  $y = L_y/2$  at various times; solid curves correspond to the run using the velocity extrapolation algorithm, dotted curves to the predictor-corrector run.

is somewhat delayed due to the extra smoothing. In the nonlinear regime, the extra smoothing gives rise to enhanced magnetic field fluctuations at  $\Omega_i t = 100$ , which occur at longer wavelengths (as shown in the bottom panel). The third set of dotted curves correspond to a run in which two smoothers are employed and the resistivity is reduced by a factor of 10. In this case, there is a larger level of short wavelength fluctuations and consequently more perpendicular ion heating. At late times, the short wavelength modes increase the overall fluctuation level dramatically, as shown in the top panel. (With only one smoothing operation at this value of the resistivity, the short wavelength modes grow up earlier and the calculation does not run to completion.) Energy conservation was monitored for the runs. In the first case (solid curves), total energy (minus the energy in the uniform magnetic field) decreases by 1.3% by the end of the run. In the second case, with extra smoothing, the energy decrease is reduced to -0.75%. In the third case, in which the resistivity is reduced, the total energy increases by 9.6%, evidently due to the enhanced levels of short wavelength fluctuations and associated ion heating.

Figure 4 shows similar tests for predictor-corrector runs in which only the resistivity is changed. The dashed curves correspond to the same case shown in the Fig. 1 with  $\eta = 10^{-6}$ ; the dashed lines correspond to a run in which the resistivity is reduced by a factor of 10. The time histories of the magnetic field fluctuations and parallel ion heating agree quite well in the two calculations. The perpendicular ion heating increases by about 20% when the resistivity is

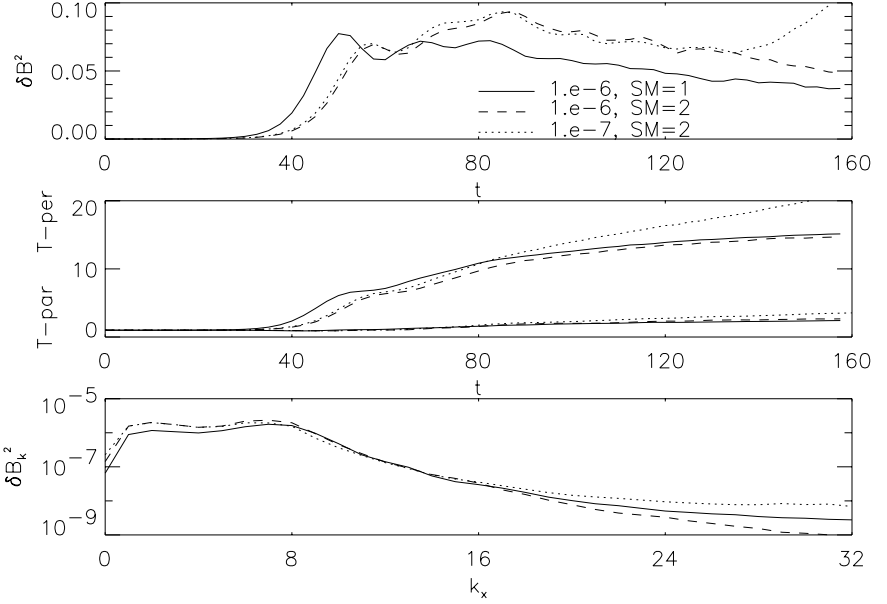


**Fig. 3.** Comparison of simulation results using the velocity extrapolation algorithm, in the same format as Fig. 1 for three runs: (solid curves)  $\eta = 10^{-6}$  with one smoothing of the source terms each time step, (dashed curves)  $\eta = 10^{-6}$  with two smooths, and (dotted lines)  $\eta = 10^{-7}$  with two smooths.

reduced, again due to the increased level of short wavelength fluctuations, as shown in the bottom panel. Energy in the system for the higher resistivity case is reduced by about 2.9% by the end of the run. In the lower resistivity case, due to the excitation of short wavelength modes, the total energy increases by about 4.5%.

For a second test problem, we compare results of 2-D hybrid simulations with those from Hall-MHD calculations for reconnection in a (Harris) current sheet. As one can see from the generalized Ohm's law (3), the electric field responsible for reconnection can arise from any of the last three terms:

$$\mathbf{E} = -\frac{\mathbf{V}_e \times \mathbf{B}}{c} - \frac{\nabla \cdot \mathbf{P}_e}{q_i n_i} + \eta \mathbf{J} - \frac{m_e}{e} \frac{d\mathbf{V}_e}{dt}. \quad (34)$$

In many hybrid calculations with  $m_e = 0$ , one uses a localized resistivity so that the consequences of reconnection in 3-D [49] or in a large 2-D tail configuration [50]–[54] can be explored. We have already discussed how to include the last term if  $m_e \neq 0$ . If one chooses to assume  $m_e = 0$  and not to insert a large localized resistivity, one needs to include, in both the hybrid (and Hall-MHD) calculations, the full electron pressure tensor in (34) in order to initiate the reconnection process [55]–[57]. The electron pressure is advanced via the following

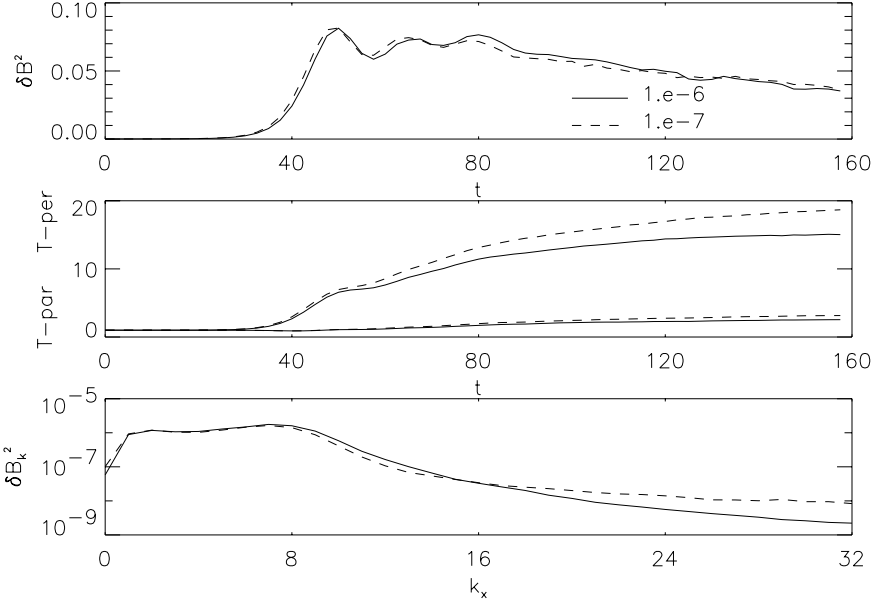


**Fig. 4.** Comparison of predictor/corrector calculations, in the same format as Fig. 1, for runs with normalized resistivities of  $\eta = 10^{-6}$  (solid curves) and  $10^{-7}$  (dashed curves).

equation that comes from a moment expansion of the Vlasov equation:

$$\begin{aligned} \frac{\partial \underline{\mathbf{P}}_e}{\partial t} = & -\mathbf{V}_e \cdot \nabla \underline{\mathbf{P}}_e - \underline{\mathbf{P}}_e \nabla \cdot \mathbf{V}_e - \underline{\mathbf{P}}_e \cdot \nabla \mathbf{V}_e - (\underline{\mathbf{P}}_e \cdot \nabla \mathbf{V}_e)^T \\ & - \Omega_e [\underline{\mathbf{P}}_e \times \hat{\mathbf{b}} + (\underline{\mathbf{P}}_e \times \hat{\mathbf{b}})^T] - \nabla \cdot \underline{\mathbf{Q}}, \end{aligned} \quad (35)$$

where  $\hat{\mathbf{b}} = \mathbf{B}/B_o$  and the superscript  $T$  indicates the transpose matrix. The term in square brackets involves the electron mass; it can either be treated implicitly, or combined with the last term, which is then replaced by a phenomenological relaxation term that models rapid electron-scale processes that reduce the non-gyrotropicity:

$$\Rightarrow -\frac{\Omega_e}{\tau} (\underline{\mathbf{P}}_e - p_e \underline{\mathbf{1}}), \quad (36)$$

where  $p_e = \frac{1}{3} \text{Tr}(\underline{\mathbf{P}}_e)$  and  $\tau \sim 1$  is on the order of electron cyclotron time.

The simulations are performed in the  $(x, y)$  plane in which  $\hat{x}$  is the direction normal to the sheet and  $\hat{y}$  is along the sheet. An initial perturbation to the Harris equilibrium  $B_y = B_o \tanh\{[x - l_x/2]/\alpha\}$  is employed, where  $l_x$  is the width of the simulation domain and  $\alpha$  is the half-thickness of the current sheet. The perturbed normal magnetic field  $B_x \sim \sin\{2\pi[y - l_y/2]/l_y\} \exp\{-[x - l_x/2]^2/\alpha^2\}$ , where  $l_y$  is the length of the simulation domain, ensures the system evolves into a non-linear stage quickly. The boundary conditions are periodic on the  $y$ -boundaries;

on the  $x$ -boundaries the velocity and field components transverse to the local magnetic field (i.e., the  $x$  and  $z$  components) vanish.

For the hybrid simulations the spatial sizes are  $10 \times 10 (c/\omega_i)^2$  (for a current sheet with half thickness  $\alpha = 0.4 c/\omega_i$ ) and  $20 \times 20 (c/\omega_i)^2$  (for  $\alpha = 0.8 c/\omega_i$ ), both consisting of  $128 \times 128$  grids; the initial perturbation amplitudes are  $B_x/B_o = 0.15$  and  $0.3$ , respectively. The lobe plasma beta is  $0.2$  and the initial ion-to-electron temperature ratio is  $T_i/T_e = 5$ . The simulations include a uniform background ion population (20 background ions per grid) whose temperature is the same as the sheet ions (an average of 20 sheet ions per grid).  $\omega_i$  is the ion plasma frequency based on the asymptotic plasma density at the lobe.

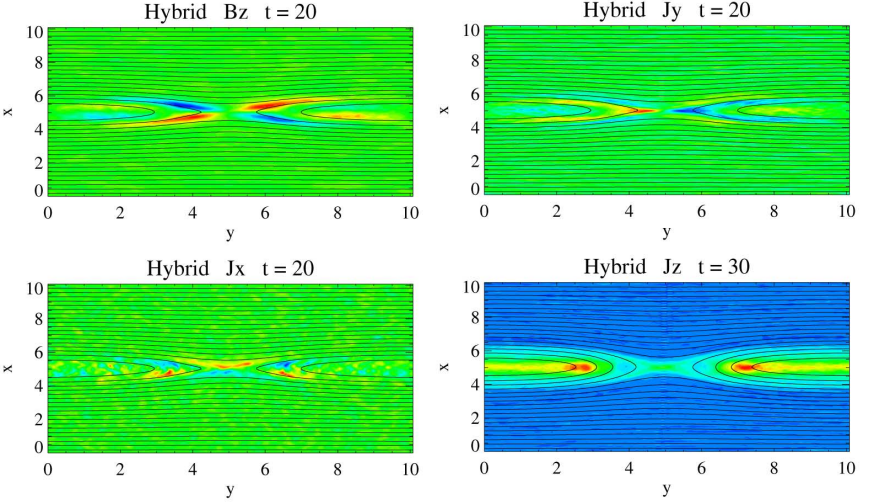


**Fig. 5.** Results of hybrid simulations of reconnection at  $\Omega_i t = 20$  and  $30$  showing color contours of  $B_z$  and the three components of the total current; magnetic field lines are overlaid on the plot.

Figure 5 shows the magnetic field and current configuration during the non-linear stage (at  $t\Omega_i = 20$  and  $30$ ) from the hybrid run (the spatial size is  $10 \times 10 (c/\omega_i)^2$  and  $\alpha = 0.4 c/\omega_i$ ). Overlaid on the magnetic field lines in the simulation plane are color contours of the out-of-plane magnetic field  $B_z$  and the current densities  $J_x$ ,  $J_y$ , and  $J_z$  plotted on a linear scale.

For the  $B_z$  contour plots the direction of  $B_z$  is along  $\hat{z}$  in the red regions but along  $-\hat{z}$  in blue regions. The same color legend applies to the current density plots. Intense currents flow toward the X point along  $\hat{y}$  and  $-\hat{y}$  directions in localized regions at the center of the sheet (see the  $J_y$  plot) and diverge from the X point in the cross-sheet directions  $\hat{x}$  and  $-\hat{x}$  (seen near the X point in the  $J_x$  plot). The current pattern for  $J_x$  and  $J_y$  is consistent with the quadrupole configuration of the out-of-plane magnetic field  $B_z$ . As the reconnection proceeds, the out-of-plane current distribution evolves to a configuration in which



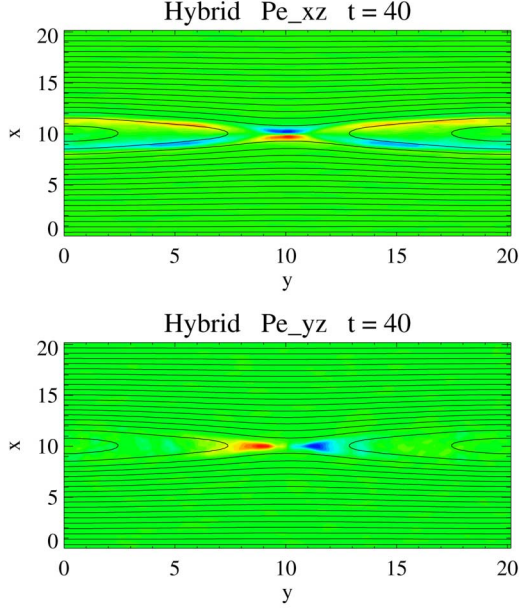


**Fig. 6.** Color contours of the  $xz$  and  $yz$  components of the electron pressure tensor from a hybrid calculation at  $\Omega_i t = 40$ .

$J_z$  intensifies at localized regions in the center of the sheet away from the X point.

Global distributions of the electron pressure tensor terms  $P_{xz}^e$  and  $P_{yz}^e$  from the hybrid simulation (the spatial size is  $20 \times 20 (c/\omega_i)^2$ ,  $\alpha = 0.8 c/\omega_i$  at  $\Omega_i t = 40$ ) are displayed in Fig. 6. The red and blue regions indicate maximum and minimum values, respectively. The magnitudes of the off-diagonal terms are relatively small: the peak values of these off-diagonal terms are a few percent of the peak values of the diagonal terms; yet their spatial configurations are clear. We will discuss their contribution to the reconnection electric field following the examination of the electric field configuration.

Next, we compare the hybrid and Hall-MHD simulation results for the 2-D reconnection problem. The Hall-MHD calculations use the same basic assumptions/equations and the same electric field and the electron pressure tensor model as in the hybrid calculations. Thus Eqs. (3) - (6) and Eqs. (32) and (33) remain the same. However, the ion kinetic treatment for each individual ion particle in Eqs. (35) and (36) is replaced with a fluid moment description in the Hall-MHD calculations. The momentum equation,

$$nm_i \frac{\partial \mathbf{V}_i}{\partial t} = -nm_i (\mathbf{V}_i \cdot \nabla) \mathbf{V}_i - \nabla p_i - \nabla \cdot \mathbf{P}_e + \frac{\mathbf{J} \times \mathbf{B}}{c}, \quad (37)$$

describes the ion fluid motion. As in most fluid simulations, a scalar ion pressure  $p_i$  is used, and thus ion finite Larmor radius effects are not modeled. The plasma

density  $n$  is computed from the continuity equation

$$\frac{\partial n}{\partial t} = -\nabla \cdot (n \mathbf{V}_i), \quad (38)$$

and  $p_i$  is obtained from

$$\frac{\partial p_i}{\partial t} = -\nabla \cdot (\mathbf{V}_i p_i) - (\gamma - 1)p_i(\nabla \cdot \mathbf{V}_i) \quad (39)$$

where  $\gamma = 5/3$  is the ratio of the specific heats.

The Hall-MHD code used here was developed with numerical methods similar to those used in conventional hybrid codes [12][36][56] so that direct comparison of the results of the two codes could more easily be carried out. Spatial grid quantities in the code are defined on the same set of staggered finite-difference meshes as described in section B and the time differencing follows a conventional staggered leapfrog method. The magnetic field  $\mathbf{B}$  is advanced in time using a fourth-order Runge-Kutta scheme with subcycling [36]. In each time step used to advance the fluid moments (velocity, density, and pressure), five to ten substeps are used, typically, to update the fields. A smoothing routine is used instead of the conventional second-order viscosity (i.e.,  $\sim \nu \nabla^2 \mathbf{V}$ ); a sixth order hyperviscous dissipation,  $\sim \nu (\nabla_x^6 + \nabla_y^6) \mathbf{B}$ , is employed in the magnetic field equation to damp out fluctuations on very short spatial scales. The Hall-MHD simulations use the same boundary conditions and simulation parameters. Since the fluid code runs relatively quickly,  $256 \times 256$  grids are used for the  $20 \times 20$   $(c/\omega_i)^2$  run for a better resolution.

Figure 7 shows a comparison of the global configuration of the electric field components  $E_y$  and  $E_z$  obtained from the hybrid run (left panels) and the Hall-MHD run (right panels). Since reconnection proceeds faster in the Hall-MHD

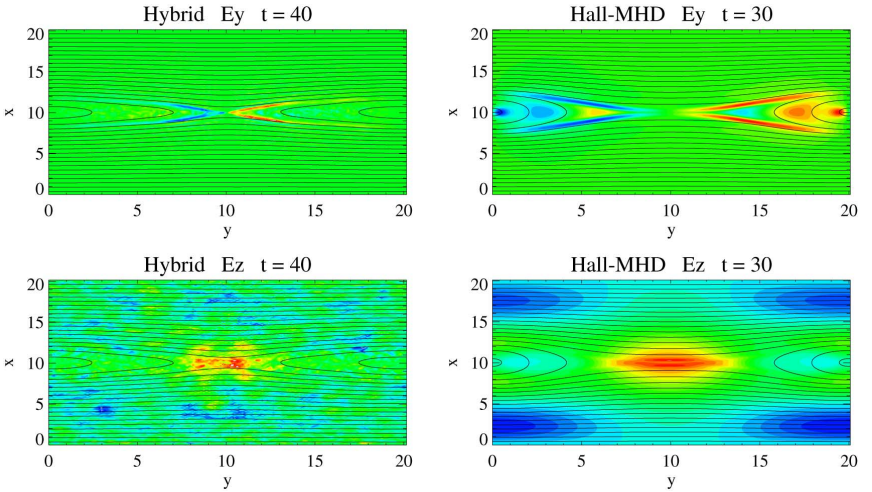


**Fig. 7.** Comparison of color contours of the electric field components  $E_y$  and  $E_z$  from hybrid (left panels) and Hall-MHD (right panels) simulations at comparable times.

run due to the absence of noise, the hybrid results at  $t\Omega_i = 40$  are compared with the Hall-MHD results at  $t\Omega_i = 30$ . The color legend is the same as in Fig. 6, i.e.,  $E_y$  and  $E_z$  have positive values in the red regions and negative values in the blue regions. General agreement is seen in the two calculations. Both runs show that the  $E_y$  component pointing away from the X point is enhanced in thin localized regions. These regions of strong  $E_y$  diverge from the X point and then follow the magnetic field lines at the edge of the sheet. The out-of-plane electric field  $E_z$  is significant mainly in the near-X-point region. The term  $-\mathbf{V}_e \times \mathbf{B}$  in Eq. (31) provides the main contribution to the global electric fields, except at the X point where the magnetic field vanishes. Eq. (31) indicates that at the X point spatial gradients of the off-diagonal electron pressure tensor terms  $-(\partial P_{xz}^e/\partial x + \partial P_{yz}^e/\partial y)$  provide a finite contribution to the  $E_z$  field (note that both  $\eta$  and  $m_e$  are set to zero). Thus this collisionless electron viscous effect plays the role of the conventional localized resistivity at the X point.

Overall agreement between the hybrid and Hall-MHD calculations is found from results of the 2-D reconnection problem in the reconnection rate, the global configuration of the currents and the fields, and the properties of the electron pressure [58]. However, in the Hall-MHD code ion dynamics are described by the ion momentum equation with a scalar ion pressure. Thus, ion finite Larmor radius effects contained in the off-diagonal terms of the ion pressure tensor are not modeled in the Hall-MHD code. This results in a significant difference in the spatial configuration of the out-of-plane ion velocity  $v_z$  from the two types of simulations as illustrated in Fig. 8: The  $v_z$  structure from the hybrid simulation (bottom panel) shows a reduction of the ion  $z$ -momentum at the X point as reconnection proceeds; in contrast,  $v_z$  from the Hall-MHD run (top panel) is peaked at the X point at this time ( $t\Omega_i = 20$ ) and remains so peaked to the end of the run. It is shown that the ion finite Larmor radius effects are important to correctly model the ion out-of-plane momentum transport from the X point and can be modeled efficiently in Hall-MHD simulations in a predictor/corrector manner that uses particle ions to implement the ion gyro-radius corrections [59][60].

## 2.4 Global Hybrid Simulations

As stated in previous sections of this paper and illustrated in the references, hybrid simulations have been conducted and shown to be extremely beneficial in theoretical investigations of the bow shock, foreshock, magnetosheath, magnetopause, slow shocks in the magnetotail and wave particle interactions in the plasma sheet boundary layer. An overwhelming majority of these studies have been in the form of 1-D or planar 2-D simulations with specific emphasis on one of these topics. The results have clearly established the significance of ion kinetic physics in the temporal and spatial structure of these regions of geospace. By noting that these regions fall in the outer part of the magnetosphere (i.e.  $R > 5 - 6R_E$ ) and that they are not heavily influenced by the ionospheric interactions or plasmas, we can construct a global model that would allow for a more comprehensive investigation of these regions. Specifically, this would allow

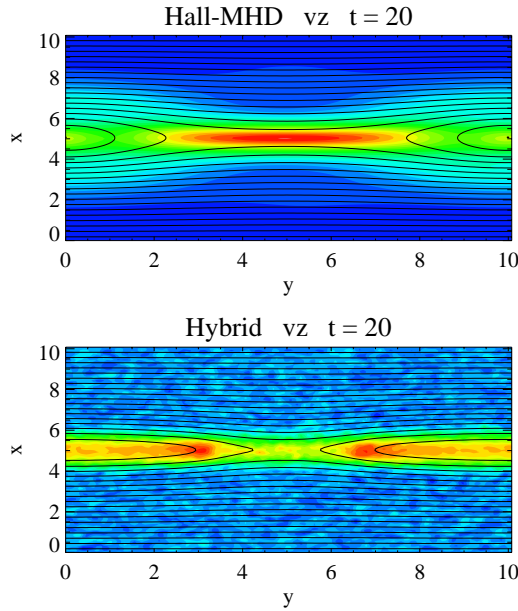


**Fig. 8.** Color contours of the ion  $z$ -velocity component at comparable times in Hall-MHD (top panel) and hybrid (bottom panel) simulations, showing differences at the X-point due to finite ion-gyroradius effects.

taking into account curvature and nonlocal effects as well as coupling between various parts of the outer magnetosphere (e.g., see [16]). While two- and three-dimensional global hybrid simulations have been performed to investigate the interaction between solar wind and Venus or Mars [61]–[63], the interaction is primarily with the respective ionospheres, where solar wind massloading is the dominant process. Also, the size of the interaction region is considerably smaller in comparison to the size of the Earth’s magnetosphere, thereby making the CPU and memory requirements more manageable, even for computers of a decade ago. In contrast to Venus and Mars, a full investigation of the Earth’s magnetosphere requires the inclusion of both its intrinsic magnetic field as well as the ionosphere. This, plus the large size of the magnetosphere, makes global hybrid simulations of this system considerably more complex and computationally more demanding.

A schematic of the global solar-wind magnetosphere simulation model is illustrated in Fig. 9. The hybrid simulations described here are two-dimensional in space, while all three components of the electromagnetic fields and ion velocities are retained [16][64]. Both the predictor-corrector field solver and ion velocity extrapolation methods described in subsection 2.B have been implemented, although the latter method is used commonly to reduce computation time. Due to the 2-D nature of the calculations, the Earth’s magnetic field is represented by a line-dipole (see, e.g., [65]), which is placed within the simulation box at an arbitrary point. This dipole forms the center of a circular (Inner) region, which

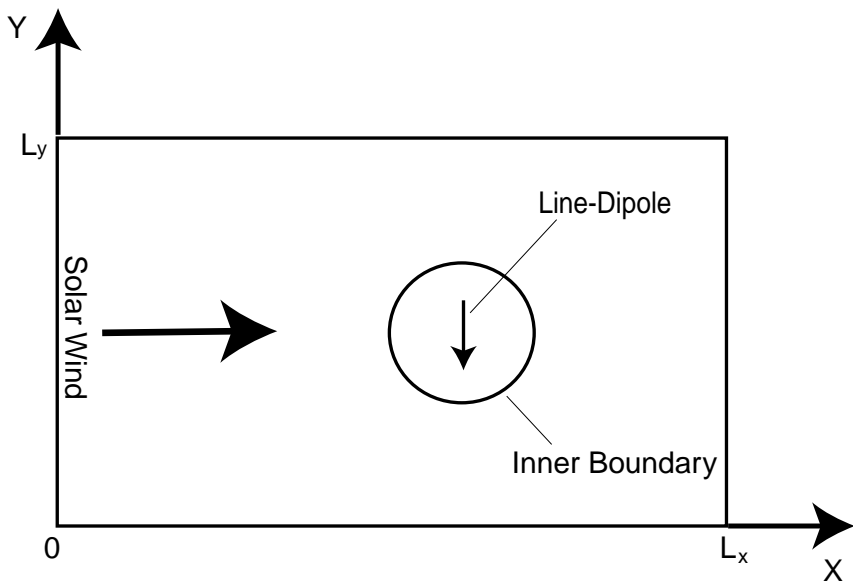


**Fig. 9.** The 2-D model used for global simulations. The solar wind is injected from the left boundary continuously during the run. The Earth’s magnetic field is represented by a line-dipole that is placed at the center of a circular region which falls outside of the simulation domain.

falls outside of the simulation domain in that all particles crossing the “Inner Boundary” are lost and the electromagnetic fields are not solved for. This region represents the inner part of the magnetosphere that the current model does not appropriately describe; a similar approach is also taken in MHD simulations. Within the Inner Region, the electric field is set to zero and the magnetic field is kept at a constant level, which either corresponds to the dipole field strength at the Inner Boundary or is simply set to zero. More sophisticated sets of boundary conditions for the particles and the electromagnetic fields at the Inner Boundary could be applied to model magnetosphere-ionosphere coupling. The solar wind plasma is initially distributed within the simulation box and is also continuously injected from the  $X = 0$  (left) boundary. This plasma is allowed to leave the system from all three remaining boundaries. The interplanetary magnetic field (IMF) is either in  $X$ - $Y$  or  $X$ - $Z$  plane making an arbitrary angle with the  $X$ -axis. The electric field at the  $X = 0$  boundary is set to the value of the motional electric field ( $\mathbf{V} \times \mathbf{B}$ ) in the solar wind. The remaining three boundaries have open or floating field boundary conditions in order to allow various waves and disturbances to leave the system. Specifically, the normal component of the electric field is set to zero on these boundaries, while the transverse components of the electric field are continuous across them. Typically, the cell size is the proton inertial length in the solar wind, which corresponds to  $\sim 100$  km. The choice of time step varies from run to run depending on the solar wind conditions and the

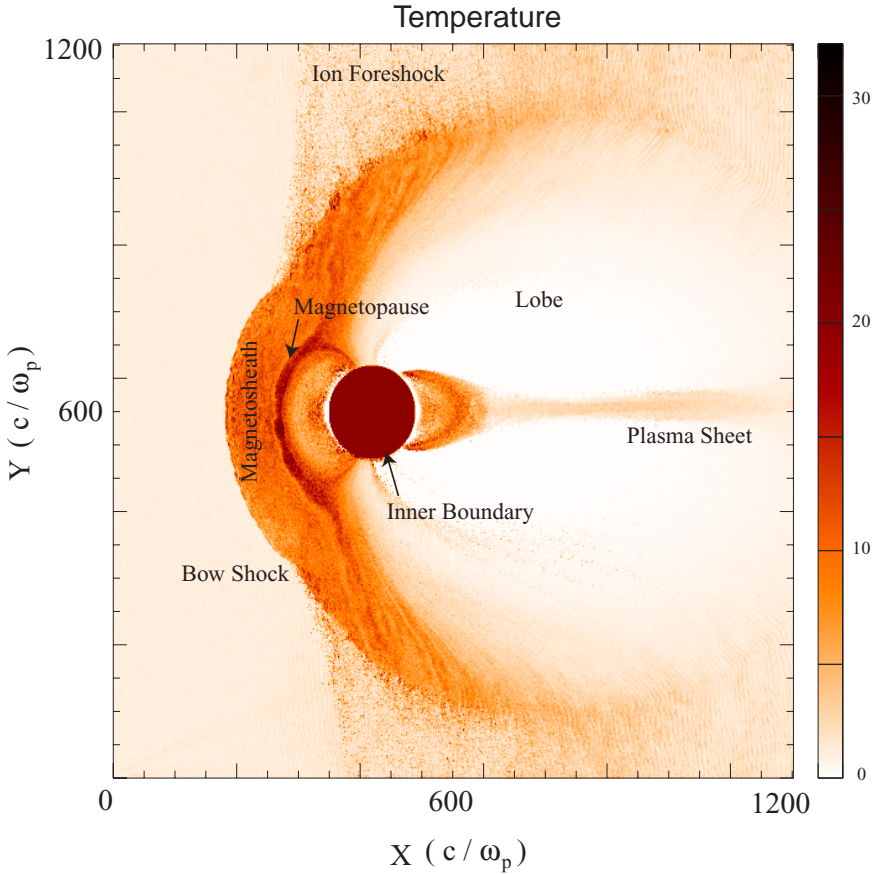


**Fig. 10.** Ion temperature as a function of  $X$  and  $Y$  in a representative global hybrid simulation. As denoted, regions representing various parts of the outer magnetosphere are formed in the simulations. The size of the simulation is roughly  $19R_E \times 19R_E$ .

dipole field strength. Typically, however, the time steps needed for numerical stability are much smaller than what one might estimate based on cell size and solar wind velocity.

Although initially the plasma is uniformly distributed in the simulation box, the evolution of the system in time results in the formation of regions and boundaries representing various parts of the outer magnetosphere. This is illustrated in Fig. 10, which shows the ion temperature, as a function of  $X$  and  $Y$ , for a representative run. In this run, the IMF lies in the  $X$ - $Y$  plane and is almost perpendicular to the  $X$ -axis ( $\theta = 85^\circ$ ). The figure shows the formation of the bow shock, ion foreshock, magnetosheath, magnetopause, the lobe and the plasma sheet. In this run, the simulation box is 1200 ion inertial lengths (in the solar wind) in  $X$  and  $Y$  directions and consists of 1,440,000 cells. Initially, each cell has 9 macroparticles but this number changes as various parts of the magnetosphere

with corresponding different plasma densities are formed. Assuming the ion inertial length to be 100 km, the size of the simulation box is about  $19R_E \times 19R_E$ , which is clearly smaller than the actual size of the magnetosphere. Similarly, because of the 2-D nature of the simulations, the system does not necessarily reach a steady state solution. This implies that these simulations cannot be used for determining the standoff position of the various discontinuities in the magnetosphere. On the other hand, the physical scale lengths associated with these boundaries (e.g. the thickness of the bow shock or the magnetopause) are appropriately modeled [16][64] and can be compared directly with spacecraft observations. Similarly, many details of the solar wind interaction with the magnetosphere that require a kinetic treatment, such as transport at the dayside magnetosphere, are properly modeled in these simulations.

Figure 10 clearly illustrates that the simulated magnetosphere bears considerable resemblance to the actual magnetosphere. This similarity goes beyond simple appearances; examination of plasma and field properties within the simulated magnetosphere show quantitative agreement with the spacecraft observations. For example, examination of the magnetic structure of the simulated bow shock in the quasi-perpendicular geometry shows considerable similarities to that of 1-D hybrid simulations as well as magnetometer data (e.g., see [19]). Similarly, evolution of the ion distribution functions across the shock reproduce the major features expected based on theory and observations [66]. This is demonstrated in Fig. 11, which shows the ion distribution functions in the upstream (top left), within the shock layer (top and bottom right) and the downstream regions (bottom left). The distribution functions within the shock layer show the characteristic presence of the gyrating ions which come about as part of the dissipation process (e.g., [8]). Evidently, the detailed study of such features in the simulations, coupled with more highly resolved observations through clusters of spacecraft, will transform our view of the dynamic magnetosphere.

The similarity between the simulated and actual magnetosphere provides a strong argument for the general validity of the model described here and shows the considerable potential it offers in understanding the dynamic and complex behavior of the magnetosphere under various solar wind conditions. This general agreement, however, is not a guarantee that numerical artifacts do not affect the specifics of a particular run, and the daunting task of assuring the physical nature of the results is a major part of the simulator's overall activities.

In a given global hybrid simulation of the magnetosphere, the simulation domain consists of many distinct regions differing in magnetic and plasma parameters. The usual tests devised for simpler systems to assess the significance of numerical artifacts in a given simulation run (e.g., conservation of energy, Courant condition) are inadequate in the highly inhomogeneous but coupled magnetospheric system. For instance, it can occur that results in one region of the simulation domain are physical but the results in another region are not. This is because the plasma and field properties change considerably within the magnetosphere (both actual and simulated), and therefore numerical conditions that are satisfied in one region may not be satisfied in another. An example of

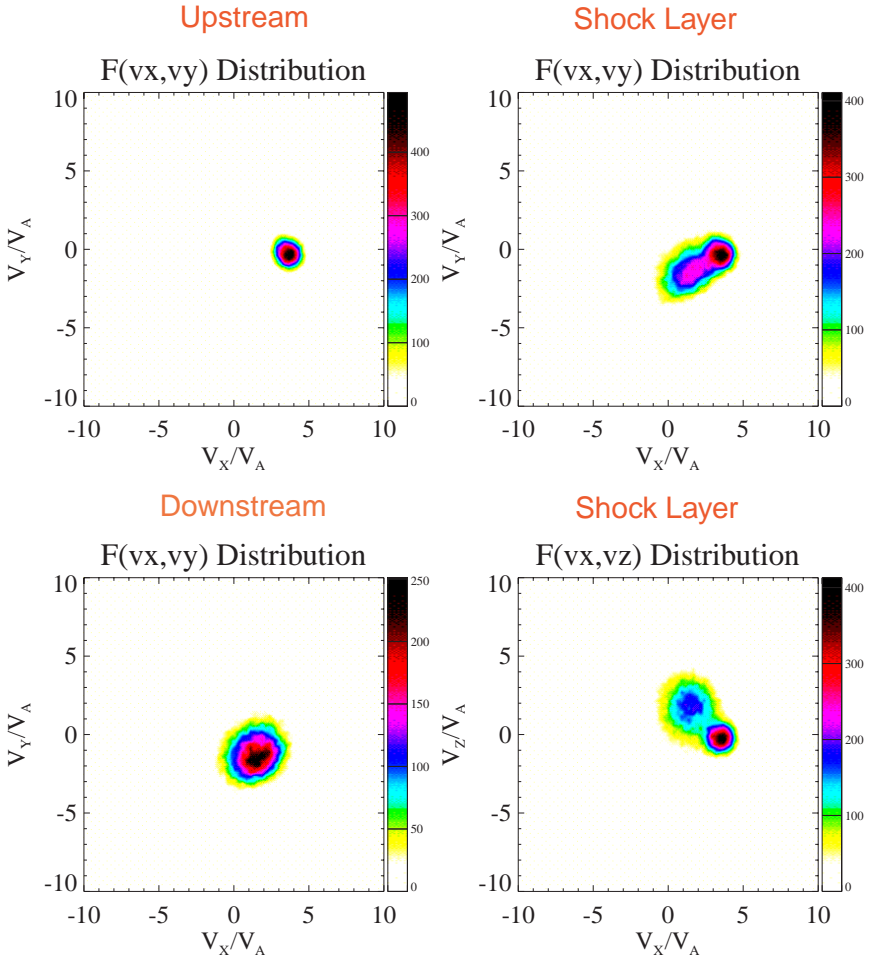


**Fig. 11.** Evolution of the ion distribution function across the quasi-perpendicular portion of the shock in a global simulation. This evolution is consistent with spacecraft observations at the bow shock and is similar to that seen in 1- and 2-D local hybrid simulations.

this is the drastic change in the plasma density from the magnetosheath into the lobe, which results in change in proton inertial length by an order of magnitude. In the case of the simulated lobe, the number of macroparticles in a cell may be one, or even less, requiring additional provisions to assure numerical stability. Since the hybrid algorithm does not contain electrostatic effects, the particle density in a given cell is never allowed to go below a certain base level. In the case of a simulated lobe, the presence of a cold, tenuous, and stationary plasma in the tail is assumed, much like the real magnetosphere; however, the plasma density in a cell is not allowed to fall below 5% of the solar wind density. Given the complexities involved, the best way of assuring the physical nature of the



results is through conducting many test runs and detailed examination of the results. This makes the process quite time consuming, but fortunately with the ever-increasing speed of the computers, this task is becoming more and more manageable.

### 3 Hybrid Codes: Future

In this tutorial, we also speculate on the future development and use of hybrid codes for space physics applications, as is already evident to some degree from the many papers at ISSS-6. We can see significant progress occurring in five general areas [12][19][67]: (1) larger and more complex simulations, (2) inclusion of more physics, (3) improvements in diagnostics for better physical insight and comparison with data, (4) algorithm development for massively parallel computers, and (5) linking hybrid and fluid codes together. Some examples of recent past progress and future work in these areas include the following.

(1) The availability of faster CPUs, more memory, etc. will lead to larger scale simulations. Such calculations will include larger regions of space, e.g., the dayside magnetosphere [16][64], the magnetopause [17][68]–[70] and the magnetotail [50][54][71][72]. In addition, three-dimensional effects, and/or more complex multi-species problems can be investigated, such as the solar wind interaction with comets [14][73][74] unmagnetized planets [61]–[63], asteroids, etc., as well as modeling kinetic processes in the expanding solar wind [75], beyond that which is presently available. We have already shown the potential, as well as some of the difficulties, for improved understanding of nonlocal processes through global hybrid simulations in the previous section.

(2) More complex physics models may include, for example, semi-collisional plasmas, such as occur in the polar region, where the outflowing plasma is collisional near the Earth and becomes less so as it flows outward [76] and at comets. This can involve new types of collision models, such as collision-field methods in which the collision “force” is treated as a grid quantity [77][78]. We have already discussed another possibility: namely, the use of hybrid codes to understand new electron and ion kinetic effects that occur near the reconnection site, which can be modeled in Hall-MHD and MHD codes.

(3) Improvements in diagnostics are likely to come through the use of commercial products, like IDL or EnSight, as the development of major visualization tools, especially in 3-D, is far too expensive for any particular research group. Hybrid codes offer unique possibilities for development of diagnostics that examine ion distribution functions, ion-scale fluctuations, etc., which can be expressed in a form convenient for comparing with data. This will be particularly useful for understanding spatial and temporal correlations between data from several different satellites, e.g., Cluster II, and global simulations.

(4) Computers that consist of 1000’s of linked processors seem to be the most economical pathway for large scale computing. Again, these can be very expensive machines that only the largest institutions can afford or they can be a group of inexpensive PC’s or Mac’s that are ganged together [79]. Understanding how

to write algorithms that take advantage of the particular system's unique architecture can be time-consuming, but can pay off in the long run. The challenge for hybrid (and other PIC) codes on massively parallel architectures is to balance the load between processors for pushing the particles and to break up the computational domain in a convenient manner [80]. For smaller scale problems, one can use the various processors to push the particles, solve the field equations over the entire domain on one processor, and distribute the field information to the other processors [27] in a very efficient manner.

(5) Finally, there is the issue of including kinetic physics in large-scale fluid calculations for developing realistic space weather codes. The required speed of such predictive codes precludes just doing global hybrid simulations [16][64]. As we have discussed earlier, kinetic effects found from hybrid simulations can be modeled in Hall-MHD codes [58][59][60]. In turn, a Hall-MHD code can be embedded in a global MHD code [60][81], thus providing an efficient way to include kinetic effects in a large-scale fluid code. Embedding an actual hybrid simulation in an MHD code would seem to be much more complex, given the disparate time and spatial scales between an ion kinetic model and an MHD model. In principle, this might be done by running the calculations concurrently on separate machines and exchanging appropriate boundary information to initialize the hybrid calculation or to update the MHD simulation each time step. It certainly provides the ultimate "grand-challenge" problem for graduates of ISSS-6!

## Acknowledgements

At Los Alamos, this work was performed under the auspices of the Department of Energy and was supported in part by the NASA Sun Earth Connection Theory Program. Work at UCSD was performed under the auspices of California Space Institute and was supported by NSF grants ATM-9901665, ATM-0119846 and an IGPP grant from LANL. Support by the San Diego Supercomputer Center is also acknowledged.

## References

1. Auer, P.L., Kilb, R.W., Crevier, W.F. (1971): Thermalization in the Earth's bow shock. *J. Geophys. Res.*, **76**, 2927
2. Forslund, D.W., Freidberg, J.P. (1971): Theory of laminar collisionless shocks. *Phys. Rev. Lett.*, **27**, 1189
3. Mason, R.J. (1971): Computer simulation of ion-acoustic shocks: The diaphragm problem. *Phys. Fluids*, **14**, 1943
4. Chodura, R. (1975): A hybrid fluid-particle model of ion heating in high-Mach-number shock waves. *Nucl. Fusion*, **15**, 55
5. Sgro, A.G., Nielson, C.W. (1976): Hybrid model studies of ion dynamics and magnetic field diffusion during pinch implosions. *Phys. Fluids*, **19**, 126
6. Hamasaki, S., Krall, N.A., Wagner, C.E., Byrne, R.N. (1977): Effects of turbulence on theta pinch modeling by hybrid numerical methods. *Phys. Fluids*, **20**, 65
7. Hewett, D.W. (1980): A global method for solving the electron-field equations in a zero-inertial electron hybrid plasma simulation code. *J. Comput. Phys.*, **38**, 378

8. Leroy, M.M., Goodrich, C.C., Winske, D., Wu, C.S., Papadopoulos, K. (1981): Simulation of a perpendicular bow shock. *Geophys. Res. Lett.*, **8**, 1269
9. Winske, D., Leroy, M.M. (1984): Hybrid simulation techniques applied to the Earth's bow shock. In: Matsumoto, H., Sato, T. (ed) *Computer Simulations of Space Plasmas*. D. Reidel/Terra Sci., Hingham MA
10. Winske, D. (1985): Hybrid simulation codes with application to shocks and upstream waves. *Space Sci. Rev.*, **42**, 53
11. Quest, K.B. (1989): Hybrid simulation. In: Lembege, B., Eastwood, J. W. (ed) *Tutorial Courses: Third International School for Space Simulation*. Cepadues Ed., Toulouse, France
12. Winske, D., Omid, N. (1993): Hybrid codes: Methods and applications. In: Matsumoto, H., Omura, Y. (ed) *Computer Space Plasma Physics: Simulations and Software*. Terra, Tokyo
13. Pritchett, P.L. (2002): Particle-in-cell simulations of plasmas. This volume
14. Bagdonat, T., Motschmann, U. (2001): 3-D hybrid simulation of the solar wind interaction with comets. In: Buechner, J., Dum, C.T., Scholer, M. (ed) *Space Plasma Simulation: Proc. Sixth International School/Symposium ISSS-6*. Copernicus Gesellschaft, Katlenburg-Lindau, Germany
15. Lipatov, A.S. (2001): Hybrid codes with finite electron mass. In: Buechner, J., Dum, C.T., Scholer, M. (ed) *Space Plasma Simulation: Proc. Sixth International School/Symposium ISSS-6*. Copernicus Gesellschaft, Katlenburg-Lindau, Germany
16. Omid, N., Karimabadi, H., Quest, K.B. (2001): Global hybrid simulations of solar wind interaction with the magnetosphere. In: Buechner, J., Dum, C.T., Scholer, M. (ed) *Space Plasma Simulation: Proc. Sixth International School/Symposium ISSS-6*. Copernicus Gesellschaft, Katlenburg-Lindau, Germany
17. Quest, K.B., Karimabadi, H. (2001): Physics of solar wind magnetosphere interactions: 3-D hybrid simulations. In: Buechner, J., Dum, C.T., Scholer, M. (ed) *Space Plasma Simulation: Proc. Sixth International School/Symposium ISSS-6*. Copernicus Gesellschaft, Katlenburg-Lindau, Germany
18. Yin, L., Winske, D., Gary, S.P., Birn, J. (2001): Hybrid and Hall-MHD simulations of collisionless reconnection: Effects of plasma pressure tensor. In: Buechner, J., Dum, C.T., Scholer, M. (ed) *Space Plasma Simulation: Proc. Sixth International School/Symposium ISSS-6*. Copernicus Gesellschaft, Katlenburg-Lindau, Germany
19. Winske, D., Omid, N. (1996): A nonspecialist's guide to kinetic simulations of space plasmas. *J. Geophys. Res.*, **101**, 17287
20. Pritchett, P.L. (2000): Particle-in-cell simulations of magnetosphere electrodynamics. *IEEE Trans. Plasma Sci.*, **28**, 1976
21. Omura, Y., Huba, J.D., Winske, D. (1999): Theory and simulations of nonlinear kinetic processes in space plasmas. In: Stone, W.R. (ed) *The Review of Radio Science 1996–1999*. Oxford Univ. Press, Oxford
22. Lipatov, A.S. (2001): *The Hybrid Multiscale Simulation Technology*. Springer-Verlag, Heidelberg, Germany
23. Vu, H.X., Brackbill, J.U. (1992): CELEST1D: An implicit fully kinetic model for low frequency electromagnetic plasma simulation. *Comput. Phys. Comm.*, **69**, 253
24. Oppenheim, M., Otani, N., Ronchi, C. (1996): Saturation of the Farley-Buneman instability via nonlinear electron  $E \times B$  drifts. *J. Geophys. Res.*, **101**, 17273
25. Mankofsky, A., Sudan, R.N., Denavit, J. (1987): Hybrid simulation of ion beams in background plasma. *J. Comput. Phys.*, **70**, 89
26. Omelchenko, Yu.A., Sudan, R.N. (1997): A 3-D Darwin-EM hybrid PIC code for ion ring studies. *J. Comput. Phys.*, **133**, 146

27. Vu, H.X. (1998): A massively parallel three-dimensional hybrid code for simulating ion-driven parametric instabilities. *J. Comput. Phys.*, **144**, 257
28. Birdsall, C.K., Langdon, A.B. (1985): *Plasma Physics Via Computer Simulation*. McGraw-Hill, New York
29. Swift, D.W. (1995): Use of a hybrid code to model the Earth's magnetosphere. *Geophys. Res. Lett.*, **22**, 311
30. Byers, J.A., Cohen, B.I., Condit, W.C., Hanson, J.D. (1978): Hybrid simulations of quasi-neutral phenomena in magnetized plasmas. *J. Comput. Phys.*, **27**, 363
31. Harned, D.S. (1982): Quasineutral hybrid simulation of macroscopic plasma phenomena. *J. Comput. Phys.*, **47**, 452
32. Winske, D., Quest, K.B. (1986): Electromagnetic ion beam instabilities: Comparison of one- and two-dimensional simulations. *J. Geophys. Res.*, **91**, 8789
33. Brecht, S.H., Thomas, V.A. (1988): Multidimensional simulations using hybrid particle codes. *Computer Phys. Comm.*, **48**, 135
34. Fujimoto, M. (1991): *Instabilities in the magnetopause velocity shear layer*. Thesis, U. Tokyo
35. Thomas, V.A., Winske, D., Omidi, N. (1990): Reforming supercritical quasi-parallel shocks: 1. One- and two-dimensional simulations. *J. Geophys. Res.*, **95**, 18809
36. Winske, D., Quest, K.B. (1988): Magnetic field and density fluctuations at perpendicular supercritical collisionless shocks. *J. Geophys. Res.*, **93**, 9681
37. Matthews, A.P. (1994): Current advance method and cyclic leapfrog for 2-D multispecies hybrid plasma simulations. *J. Comput. Phys.*, **112**, 102
38. Horowitz, E.J., Shumaker, D.E., Anderson, D.V. (1989): QN3D: A three-dimensional quasi-neutral hybrid particle-in-cell code with applications to the tilt instability in field reversed configurations. *J. Comput. Phys.*, **84**, 279
39. Terasawa, T., Hoshino, M., Sakai, J.I., Hada, T. (1986): Decay instability of finite amplitude circularly polarized Alfvénwaves: A numerical simulation of stimulated Brillouin scattering. *J. Geophys. Res.*, **91**, 4171
40. Kazeminezhad, F., Dawson, J.M., Leboeuf, J.N., Sydora, R., Holland, D. (1992): A Vlasov particle ion zero mass electron model for plasma simulations. *J. Comput. Phys.*, **102**, 277
41. Hewett, D.W., Nielson, C.W. (1978): A multidimensional quasineutral plasma simulation model. *J. Comput. Phys.*, **29**, 219
42. Shay, M., Drake J.F., Denton, R.E., Biskamp, D. (1998): Structure of the dissipation region during collisionless magnetic reconnection. *J. Geophys. Res.*, **103**, 9165
43. Kuznetsova, M.M., Hesse, M., Winske, D. (1998): Kinetic quasi-viscous and bulk flow inertia effects in collisionless magnetotail reconnection. *J. Geophys. Res.*, **103**, 199
44. Omidi, N., Winske, D. (1992): Kinetic structure of slow shocks: Effects of the electromagnetic ion/ion cyclotron instability. *J. Geophys. Res.*, **97**, 14801
45. Winske, D., Omidi, N. (1992): Electromagnetic ion/ion cyclotron instability: Theory and simulations. *J. Geophys. Res.*, **97**, 14779
46. Cremer, M., Scholer, M. (1999): Collisionless slow shocks in magnetotail reconnection. *Geophys. Res. Lett.*, **26**, 2709
47. Cremer, M., Scholer, M. (2000): Structure of the reconnection layer and the associated slow shocks: Two-dimensional simulations of a Riemann problem. *J. Geophys. Res.*, **105**, 27621
48. Daughton, W., Gary, S.P., Winske, D. (1999): Electromagnetic proton/proton instabilities in the solar wind: Simulations. *J. Geophys. Res.*, **104**, 4657

49. Nakamura, M.S., Fujimoto, M. (1998): A three-dimensional hybrid simulation of magnetic reconnection. *Geophys. Res. Lett.*, **25**, 2917
50. Krauss-Varban, D., Omidi, N. (1995): Large-scale hybrid simulations of the magnetotail during reconnection. *Geophys. Res. Lett.*, **22**, 3271
51. Kuznetsova, M.M., Hesse, M., Winske, D. (1996): Ion dynamics in a hybrid simulation of magnetotail reconnection. *J. Geophys. Res.*, **101**, 27351
52. Nakabayashi, J., Machida, S. (1997): Electromagnetic hybrid code simulation of magnetic reconnection: Velocity distribution functions of accelerated ions. *Geophys. Res. Lett.*, **24**, 1339
53. Nakamura, M.S., Fujimoto, M. (1998): Ion dynamics and resultant velocity space distributions in the course of magnetotail reconnection. *J. Geophys. Res.*, **103**, 4531
54. Lottemoser, R.F., Scholer, M., Matthews, A.P. (1998): Ion kinetics in magnetic reconnection: Hybrid simulations. *J. Geophys. Res.*, **103**, 4547
55. Hesse, M., Winske, D. (1993): Hybrid simulations of collisionless ion tearing. *Geophys. Res. Lett.*, **20**, 1207
56. Hesse, M., Winske, D. (1994): Hybrid simulations of collisionless reconnection in current sheets. *J. Geophys. Res.*, **99**, 11177
57. Hesse, M., Winske, D., Kuznetsova, M.M. (1995): Hybrid modeling of collisionless reconnection in two-dimensional current sheets: Simulations. *J. Geophys. Res.*, **100**, 21815
58. Yin, L., Winske, D., Gary, S.P., Birn, J. (2001): Hybrid and Hall-MHD simulations of collisionless reconnection: Dynamics of the electron pressure tensor. *J. Geophys. Res.*, **106**, 10761
59. Yin, L., Winske, D., Gary, S.P., Birn, J. (2001): Particle Hall-MHD simulation of collisionless reconnection: Finite ion gyro-orbit correction. *Geophys. Res. Lett.*, **28**, 2173
60. Yin, L., Winske, D., Gary, S.P., Birn, J. (2002): Hybrid and Hall-magnetohydrodynamics simulations of collisionless reconnection: Effect of the ion pressure tensor and particle Hall-magnetohydrodynamics. *Phys. Plasmas*, **9**, 2575-2584
61. Brecht, S.H., Ferrante, J.R. (1991): Global hybrid simulation of unmagnetized planets: Comparison of Venus and Mars. *J. Geophys. Res.*, **96**, 11209
62. Brecht, S.H., Ferrante, J.R., Luhmann, J.G. (1993): Three-dimensional simulations of the solar wind interaction with Mars. *J. Geophys. Res.*, **98**, 1345
63. Brecht, S.H. (1997): Hybrid simulations of the magnetic topology of Mars. *J. Geophys. Res.*, **102**, 4743
64. Omidi, N., Karimabadi, H., Krauss-Varban, D. (1998): Hybrid simulation of the curved dayside magnetopause during southward IMF. *Geophys. Res. Lett.*, **25**, 3273
65. Ogino, T. (1993): Two-dimensional MHD code. In: Matsumoto, H., Omura, Y. (ed) *Computer Space Plasma Physics: Simulations and Software*. Terra, Tokyo
66. Schkopke, N., Paschmann, G., Bame, S.J., Gosling, J.T., Russell, C.T. (1983): Evolution of ion distributions across the nearly perpendicular bow shock: Specularly and non-specularly reflected-gyrating ions. *J. Geophys. Res.*, **88**, 6121
67. Dawson, J.M. (1999): Role of computer modeling of plasmas in the 21st century. *Phys. Plasmas*, **6**, 4436
68. Lin, Y., Xie, H. (1997): Formation of reconnection layer at the dayside magnetopause. *Geophys. Res. Lett.*, **24**, 3145
69. Xie, H., Lin, Y. (2000): Two-dimensional hybrid simulation of the dayside reconnection layer and associated ion transport. *J. Geophys. Res.*, **105**, 25171

70. Nakamura, M., Scholer, M. (2000): Structure of the magnetopause reconnection layer and of flux transfer events: Ion kinetic effects. *J. Geophys. Res.*, **105**, 23179
71. Lin, Y., Swift, D.W. (1996): A two-dimensional hybrid simulation of the magnetotail reconnection layer. *J. Geophys. Res.*, **101**, 19859
72. Scholer, M., Lottermoser, R.F. (1998): On the kinetic structure of the magnetotail reconnection layer. *Geophys. Res. Lett.*, **25**, 3281
73. Galeev, A.A., Lipatov, A.S., Sagdeev, R.Z. (1987): Two-dimensional numerical simulation of the relaxation of cometary ions and MHD turbulence in the flow of the solar wind around a cometary atmosphere. *Sov. J. Plasma Phys.*, **13**, 323
74. Omidi, N., Winske, D. (1990): Steepening of magnetosonic waves into shocklets: Simulations and consequences for planetary shocks and comets. *J. Geophys. Res.*, **95**, 2281
75. Liewer, P.C., Velli, M., Goldstein, B. (1999): Hybrid simulations of wave propagation and ion cyclotron heating in the expanding solar wind. *Space Sci. Rev.*, **87**, 257
76. Miller, R.H., Rasmussen, C.E., Gombosi, T.I., Khazanov, G.V., Winske, D. (1993): Kinetic simulation of plasma flows in the inner magnetosphere. *J. Geophys. Res.*, **98**, 19301
77. Jones, M.E., Lemons, D.S., Mason, R.J., Thomas, V.A., Winske, D. (1996): A grid-based Coulomb collision model for PIC codes. *J. Comput. Phys.*, **123**, 169
78. Thomas, V.A. (1997): Modeling combined collisional/collisionless plasma interpenetration. *IEEE Trans. Plasma Sci.*, **25**, 353
79. Decyk, V.K., Dager, D.E. (2001): How to build an AppleSeed: A parallel Macintosh cluster for numerically intensive computing. In: Buechner, J., Dum, C.T., Scholer, M. (ed) *Space Plasma Simulation: Proc. Sixth International School/Symposium ISSS-6*. Copernicus Gesellschaft, Katlenburg-Lindau, Germany
80. Liewer, P.C., Decyk, V.K. (1989): A general concurrent algorithm for plasma particle-in-cell simulation codes. *J. Comput. Phys.*, **85**, 302
81. Omidi, N., Blanco-Cano, X., Russell, C.T., Karimabadi, H., Acuna, M. (2002): Hybrid simulations of solar wind interaction with magnetized asteroids: General characteristics. *J. Geophys. Res.*, **107**, in press